

# Homogeneous abundance ratios of hydrostatic and explosive alpha-elements in globular clusters from high resolution optical spectroscopy<sup>★</sup>

Eugenio Carretta<sup>1</sup>

INAF-Osservatorio di Astrofisica e Scienza dello Spazio di Bologna, Via P. Gobetti 93/3, I-40129 Bologna, Italy

## ABSTRACT

Galactic globular clusters (GCs) were born shortly after the Big Bang. For such old stellar systems the initial mass function (IMF) at the high mass regime can never be observed directly, because stars more massive than about  $1 M_{\odot}$  have evolved since long time. However, the hydrostatic to explosive  $\alpha$ -element ratio (HEx ratio) offers a way to bypass the lack of observable high mass stars through the yields that massive stars released when exploding as supernovae, incorporated in the stars we presently observe in GCs. The HEEx ratio measures the percentage of high mass stars over the total number of stars exploding as supernovae and it is an efficient probe of the ephemeral first phases of the GC evolution. We exploited a recently completed survey to assemble a dataset of very homogeneous abundances of  $\alpha$ -elements in 27 GCs from  $[Fe/H] \sim -2.4$  to  $\sim -0.3$  dex. In agreement with previous results from APOGEE, we confirm that the HEEx ratio is indistinguishable for GCs formed in situ and accreted in the Galaxy, and that this ratio decreases with increasing metallicity. However, we posit that this trend is better explained by a metallicity-dependent IMF deficient in the highest mass stars at high metallicity, as corroborated by the declining  $[O/Mg]$  ratio as a function of the  $[Mg/H]$  ratio. At odds with the previous analysis based on APOGEE data, we detect an anti-correlation of HEEx ratio with both present day and initial GC masses. Finally, we hypothesise that in that analysis, the stars of the GC M 54 were probably confused with stars in the core of the Sagittarius dwarf galaxy, where the cluster is presently immersed.

**Key words.** Stars: abundances – Stars: atmospheres – Stars: Population II – Galaxy: globular clusters: general

## 1. Introduction

Oxygen follows hydrogen and helium as the most abundant elements in the Universe. Reactions with successive captures of He nuclei ( $\alpha$  particles) on Ne synthetise Mg, Si, Ca, and Ti (e.g. Burbidge et al. 1957), collectively known as  $\alpha$ -elements. These elements are enhanced in metal-poor stars (see Wallerstein 1962) and in particular in globular clusters (GCs) of the Milky Way (MW). This occurrence is explained with the interplay between star formation and the lifetime of stars in different mass ranges (Tinsley 1979). Massive stars evolve quickly, leading to a quick (prompt) release of copious amounts of  $\alpha$ -elements in core-collapse supernovae (CCSNe), well before the bulk of contribution by type Ia SNe, whose precursors evolve on a longer (delayed) timescale, may lower the  $[\alpha/Fe]$ <sup>1</sup> ratio raising the iron content of the yields. The level of  $\alpha$ -elements measured in a stellar system is then a probe of the efficiency of the system to produce and retain yields from massive stars before the onset of the bulk of SNe Ia.

However, the dominant nucleosynthetic channels are different for different species belonging to this group. The synthesis of O and Mg is dominated by hydrostatic burning in the outermost shells of the most massive stars (in the range  $15-30 M_{\odot}$ ) before being released by CCSNe (e.g. Weinberg et al. 2019 and

references therein). As a consequence, they are dependent on the mass of the star, with yields increasing with increasing progenitor mass, but only a weak dependence on metallicity at fixed stellar mass (e.g. Woosley and Weaver 1995, Andrews et al. 2017, Griffith et al. 2019). Explosive  $\alpha$ -elements like Si, Ca, and Ti are produced in shells lying closer to the core of massive stars. This makes their yields relatively independent of stellar mass when they are released by SNe, predominantly by CCSNe, with a lower, but significant contribution from SNe Ia (e.g. Nomoto et al. 1984).

These different properties means that the comparison of  $\alpha$ -elements produced in hydrostatic burning (O, Mg) to the abundance of explosive  $\alpha$ -elements (Si, Ca, Ti) is an efficient way to sample the high mass end of the initial mass function (IMF) of a given stellar population (e.g. McWilliam et al. 2013, Carlin et al. 2018) through the analysis of the yields incorporated in the stars we are presently observing. For GCs this is an important probe, since stars more massive than  $\sim 1 M_{\odot}$  are since long time evolved off the main sequence and are difficult to observe.

The first and most straightforward applications of this method were both for the Sagittarius dwarf galaxy (Sgr dSph). Using the  $[Mg/Fe]$  ratio as example of the hydrostatic-to-explosive abundance ratio of  $\alpha$ -elements McWilliam et al. (2013) concluded that the decline of this ratio with increasing metallicity suggests the evidence of an IMF deficient in the highest mass stars. Carlin et al. (2018), who coined the term HEEx ratio, reached similar conclusion by studying this ratio in 42 stars in the Sgr tidal stream. Both studies were based on optical high resolution spectroscopy.

Send offprint requests to: E. Carretta, eugenio.carretta@inaf.it

<sup>★</sup> Based on observations collected at ESO telescopes under programmes (see Appendix)

<sup>1</sup> We adopt the usual spectroscopic notation, *i.e.*  $[X] = \log(X_{\text{star}} - \log(X_{\odot})$  for any abundance quantity X, and  $\log \epsilon(X) = \log (N_X/N_H) + 12.0$  for absolute number density abundances.

The same approach is made more complicated in GCs by the presence of multiple stellar populations (MPs). Whereas most heavy elements show a high degree of homogeneity in GCs (e.g. Gratton et al. 2004), MPs are distinct by variations of the abundances of light elements, modified by proton-capture reactions with respect to the primordial level established in GCs by SNe (see Gratton et al. 2012, 2019 for comprehensive reviews). In the network of proton-capture reactions in H-burning at high temperature (e.g. Langer et al. 1993) the hydrostatic  $\alpha$ -elements O and Mg are both consumed to produce N and Al. Oxygen may be depleted even down to  $[\text{O}/\text{Fe}] \sim -1$  dex starting from the mean enhancement (0.3-0.4 dex) typical of GCs, and its variations are observed in almost every GCs in the MW (e.g. Carretta et al. 2010a). Depletion of Mg abundances is much more moderate, and significant variations are only observed in GCs that are metal-poor, massive, or both (Carretta et al. 2009a, Mészáros et al. 2020). Also the explosive elements Si and Ca are affected by the MPs phenomenology. In the case of Si, the changes in abundances are usually small, since the main mechanism is actually a leakage on Si from the Mg-Al cycle (e.g. Arnould et al. 1999, Yong et al. 2005). Variations in Ca, detected as small yet observable excesses with respect to unpolluted field stars of similar metallicity, are much more rare, being found in about 10% of all the surveyed GCs (Carretta and Bragaglia 2021).

A large survey of HEx ratios in GCs, as well as in halo substructures and satellites galaxies of the MW, was recently done by Horta and Ness (2025; hereinafter HN25) exploiting the APOGEE survey DR17. They used the unpolluted stellar population in GCs selecting N-poor/C-rich and Al-poor/Mg-rich stars and they favour an alternative scenario explaining the decreasing trend of HEx ratios in GCs with the metallicity with a delayed contribution of SNe Ia, leading to a higher contribution of both iron and explosive  $\alpha$ -elements.

In the present work we are taking advantage of a recently completed survey of Mg, Si, Ca, and Ti from high resolution optical spectroscopy in 16 GCs (Carretta 2026). We provide a description of the available data in Section 2, compute the HEx ratios for GCs in Section 3, and compare our results with those from the APOGEE survey (Section 4). Finally, we discuss and summarise our findings in Section 5.

## 2. Datasets

We added other 11 GCs studied by the same group in individual papers to the sample in Carretta (2026). Average abundances of oxygen and other  $\alpha$ -elements are listed in Table 1 in the first row for each GC, together with the cluster metallicity  $[\text{Fe}/\text{H}]$  on the metallicity scale by Carretta et al. (2009b) from high resolution UVES spectra. We stress that this ensemble of 27 GCs represents a very homogeneous dataset, being analysed with identical methodology. We employed the same scale of atmospheric parameters, the same line list, the same method for measurements of equivalent widths, the same reference solar abundances. All the stars (more than 2600 with Fe and at least a measured species of  $\alpha$ -elements) have membership certified by radial velocity and abundance. References for all the papers where abundances of individual stars can be retrieved (usually in electronic form at CDS) are given in Table A.1.

We adopted the classification given in Massari et al. (2019), with a few amendments as in Carretta (2026), for the birth place of GCs. In our sample, eight GCs are in situ clusters, born in the disc or bulge of the Milky Way. The other objects are thought to have formed in former external systems and afterward brought in the main Galaxy from the accretion events linked to Gaia-

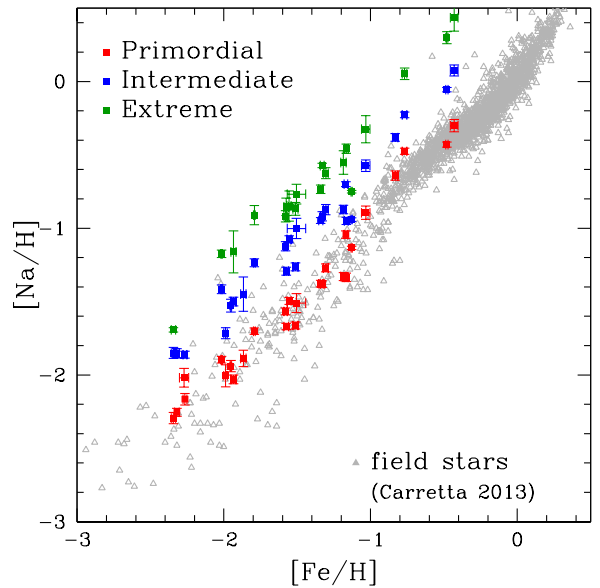


**Fig. 1.** Average abundance ratio  $[\text{Na}/\text{H}]$  as a function of metallicity for GC stars with primordial (P, red squares), intermediate (I, in blue), and extreme (E, green) composition in our GCs, superimposed to a reference sample of unpolluted field stars from Carretta (2013: grey open triangles).

Enceladus, Sequoia, the Helmi streams, Sagittarius, or the group of low orbital energy GCs of still uncertain origin.

We used field stars of the Milky Way as a reference baseline. We employed the sample of stars with good parallaxes by Gratton et al. (2003) from which we also adopt our solar reference abundances. The field stars cover the same metallicity range spanned by the GC sample and the abundances are derived from the same line list as used for GC stars. Another reference consists in 27 stars in the nucleus of the Sgr dSph from Carretta et al. (2010c). Although limited in size, this sample is useful to evaluate the behaviour of the HEx ratio in a sub-structure accreted in the Milky Way. From the comparison of the abundances, Carretta et al. (2010c) showed that the stars in the Sgr core can be distinct from those of the GC NGC 6715. While presently embedded in the Sgr core, this GC probably formed separately and plunged in the core of Sgr due to dynamical friction only at later times. The different chemistry of core stars and GC is clearly highlighted by proton-capture elements (Carretta et al. 2010c), but it seems also shared by the ratio of hydrostatic to explosive  $\alpha$ -elements (see below).

The impact of the properties of MPs is a potential problem in deriving the correct or unbiased HEx ratio for GCs. Abundance variations due to proton-capture reactions in H-burning at high temperature affect in particular the hydrostatic species O and Mg, and only to a smaller extent explosive  $\alpha$ -elements like e.g. Si and Ca (see e.g. section 1 and Carretta 2026). This potential bias can be efficiently solved by using only the unpolluted stellar component in GCs, that is the fraction of stars that still maintain the original chemical composition, before the polluters enriched the proto-cluster in ejecta processed by proton-capture reactions.

To this purpose, we adopt the criteria given in Carretta et al. (2009c) for the classification of MPs in GCs according to the Na-O anti-correlation. The unpolluted component with primordial (P) composition includes all stars with Na abundance between the minimum  $[\text{Na}/\text{Fe}]$  observed in each GC and  $[\text{Na}/\text{Fe}]_{\min} + 4\sigma$ . The polluted stars are separated into fractions with interme-

**Table 1.** Average abundances of hydrostatic and explosive  $\alpha$ -elements

GC	[O/Fe] n mean rms	[Mg/Fe] n mean rms	[Si/Fe] n mean rms	[Ca/Fe] n mean rms	[Ti/Fe] I n mean rms	[Fe/H] mean rms
0104	115 +0.152 0.179	147 +0.530 0.076	147 +0.433 0.061	147 +0.315 0.024	146 +0.394 0.036	-0.768 0.054
P only	31 +0.289 0.083	31 +0.533 0.081	31 +0.399 0.058	31 +0.310 0.023	31 +0.394 0.033	
0288	70 +0.132 0.257	107 +0.469 0.045	112 +0.389 0.029	111 +0.402 0.045	106 +0.283 0.040	-1.305 0.054
P only	23 +0.286 0.196	22 +0.465 0.043	23 +0.379 0.035	23 +0.394 0.035	23 +0.270 0.030	
0362	71 +0.091 0.189	87 +0.328 0.042	89 +0.248 0.040	91 +0.334 0.026	86 +0.172 0.037	-1.166 0.048
P only	16 +0.219 0.097	14 +0.347 0.034	15 +0.231 0.027	16 +0.340 0.030	15 +0.161 0.022	
1851	96 +0.002 0.209	123 +0.374 0.036	124 +0.383 0.029	125 +0.324 0.035	122 +0.155 0.053	-1.185 0.068
P only	30 +0.170 0.112	30 +0.393 0.034	29 +0.365 0.029	30 +0.317 0.029	30 +0.144 0.049	
1904	58 +0.078 0.205	57 +0.272 0.040	68 +0.304 0.036	67 +0.276 0.037	66 +0.131 0.042	-1.579 0.033
P only	19 +0.215 0.098	19 +0.276 0.038	19 +0.292 0.039	19 +0.274 0.033	19 +0.141 0.035	
2808	117 +0.001 0.371	139 +0.272 0.156	140 +0.296 0.054	140 +0.328 0.023	140 +0.213 0.033	-1.129 0.030
P only	42 +0.308 0.058	46 +0.384 0.041	46 +0.265 0.026	46 +0.321 0.024	46 +0.215 0.033	
3201	110 +0.125 0.286	131 +0.341 0.049	146 +0.299 0.038	150 +0.306 0.039	118 +0.082 0.037	-1.512 0.065
P only	35 +0.273 0.166	32 +0.338 0.041	35 +0.293 0.039	35 +0.293 0.035	34 +0.079 0.034	
4590	56 +0.403 0.178	62 +0.364 0.066	54 +0.423 0.057	120 +0.280 0.042	18 +0.162 0.048	-2.265 0.047
P only	19 +0.473 0.177	18 +0.350 0.065	13 +0.409 0.049	19 +0.272 0.042	8 +0.164 0.048	
4833	61 +0.243 0.270	52 +0.338 0.173	71 +0.459 0.051	78 +0.351 0.015	62 +0.167 0.023	-2.015 0.014
P only	16 +0.456 0.102	14 +0.508 0.078	16 +0.426 0.027	16 +0.349 0.018	16 +0.166 0.026	
5634	6 +0.292 0.134	7 +0.519 0.032	7 +0.295 0.031	7 +0.299 0.024	7 +0.146 0.015	-1.867 0.050
P only	3 +0.388 0.107	4 +0.512 0.047	4 +0.296 0.045	4 +0.285 0.024	4 +0.137 0.015	
5904	114 +0.139 0.282	135 +0.422 0.052	137 +0.320 0.034	138 +0.371 0.028	133 +0.181 0.027	-1.340 0.052
P only	31 +0.387 0.122	31 +0.418 0.053	31 +0.310 0.037	31 +0.369 0.032	31 +0.182 0.029	
6093	63 +0.223 0.217	70 +0.458 0.061	79 +0.354 0.031	82 +0.356 0.016	68 +0.189 0.029	-1.792 0.023
P only	18 +0.405 0.111	17 +0.461 0.048	17 +0.351 0.037	18 +0.356 0.016	18 +0.187 0.028	
6121	88 +0.218 0.118	104 +0.545 0.045	104 +0.538 0.039	104 +0.415 0.035	104 +0.281 0.033	-1.168 0.046
P only	26 +0.313 0.079	26 +0.547 0.050	26 +0.519 0.039	26 +0.412 0.031	26 +0.277 0.034	
6171	30 +0.172 0.187	33 +0.522 0.044	33 +0.524 0.049	33 +0.415 0.032	33 +0.174 0.038	-1.033 0.064
P only	10 +0.309 0.075	10 +0.533 0.028	10 +0.528 0.056	10 +0.425 0.031	10 +0.170 0.032	
6218	75 +0.281 0.275	81 +0.537 0.037	81 +0.356 0.044	81 +0.420 0.038	80 +0.251 0.024	-1.330 0.042
P only	18 +0.525 0.137	18 +0.540 0.032	18 +0.316 0.034	18 +0.410 0.047	18 +0.254 0.025	
6254	109 +0.271 0.212	129 +0.481 0.065	144 +0.314 0.057	152 +0.342 0.037	130 +0.176 0.043	-1.575 0.059
P only	33 +0.401 0.131	32 +0.519 0.067	31 +0.294 0.051	33 +0.328 0.037	33 +0.166 0.045	
6388	183 -0.071 0.229	184 +0.220 0.052	184 +0.317 0.063	185 +0.067 0.046	185 +0.275 0.096	-0.480 0.045
P only	53 +0.103 0.145	53 +0.233 0.053	53 +0.284 0.048	54 +0.053 0.050	54 +0.258 0.105	
6397	19 +0.274 0.085	97 +0.454 0.041	49 +0.337 0.037	147 +0.290 0.035	38 +0.177 0.037	-1.988 0.044
P only	4 +0.332 0.069	4 +0.467 0.040	4 +0.326 0.037	4 +0.267 0.037	4 +0.164 0.025	
6441	29 +0.040 0.180	29 +0.370 0.130	30 +0.400 0.180	29 +0.170 0.180	27 +0.320 0.180	-0.348 0.090
P only	11 +0.100 0.100	11 +0.410 0.130	11 +0.360 0.210	11 +0.110 0.170	10 +0.250 0.150	
6535	27 +0.602 0.190	24 +0.479 0.051	6 +0.418 0.035	7 +0.312 0.018	7 +0.184 0.036	-1.952 0.036
P only	8 +0.699 0.178	7 +0.495 0.035	7 +0.428 0.048	8 +0.339 0.043	6 +0.186 0.045	
6715	76 +0.070 0.344	75 +0.344 0.170	77 +0.414 0.102	77 +0.363 0.107	77 +0.166 0.137	-1.505 0.164
P only	21 +0.359 0.078	21 +0.421 0.102	21 +0.385 0.081	21 +0.307 0.083	21 +0.095 0.099	
6752	107 +0.242 0.245	125 +0.387 0.107	137 +0.476 0.062	130 +0.397 0.033	134 +0.181 0.039	-1.555 0.051
P only	26 +0.452 0.163	25 +0.457 0.058	26 +0.434 0.064	26 +0.395 0.027	24 +0.174 0.035	
6809	113 +0.251 0.191	129 +0.483 0.061	146 +0.380 0.044	152 +0.363 0.042	133 +0.147 0.056	-1.934 0.063
P only	17 +0.380 0.090	17 +0.523 0.041	17 +0.377 0.041	17 +0.360 0.052	17 +0.140 0.050	
6838	43 +0.364 0.112	51 +0.496 0.043	51 +0.391 0.051	51 +0.312 0.050	51 +0.366 0.070	-0.832 0.061
P only	12 +0.403 0.109	12 +0.499 0.042	12 +0.391 0.056	12 +0.274 0.050	12 +0.342 0.067	
7078	45 +0.308 0.187	55 +0.420 0.175	59 +0.472 0.093	82 +0.273 0.054	36 +0.219 0.040	-2.320 0.057
P only	13 +0.438 0.125	13 +0.542 0.107	10 +0.395 0.081	13 +0.254 0.053	12 +0.213 0.029	
7099	35 +0.376 0.264	33 +0.505 0.044	22 +0.367 0.058	68 +0.323 0.051	24 +0.240 0.032	-2.344 0.049
P only	12 +0.507 0.115	10 +0.511 0.035	5 +0.298 0.062	12 +0.318 0.045	8 +0.234 0.031	
Ter8	6 +0.394 0.045	6 +0.470 0.092	6 +0.248 0.095	6 +0.190 0.038	6 +0.050 0.057	-2.271 0.079
P only	6 +0.394 0.045	6 +0.470 0.092	6 +0.248 0.095	6 +0.190 0.038	6 +0.050 0.057	

Notes: for each GC, the second row lists the average abundances computed using only the P stars with primordial composition; n is the number of stars used in the averages.

ate (I) and extreme (E) composition according to their position along the Na-O anti-correlation ( $[O/Na] > -0.9$  and  $[O/Na] < -0.9$  dex respectively). Concerning the present study, what is relevant is that the P stars bear the composition of unpolluted field stars of similar metallicity, inherited essentially from SNe nucleosynthesis, as shown in Fig. 1. In this figure we plot the average  $[Na/H]$  ratios for the P, I, and E components in our sample of GCs superimposed to a reference sample of field stars from Carretta (2013). The P stars well matches the locus of the unpolluted stars. The good correlation between abundances of O and Mg in MPs ( $p\text{-value} < 1.0 \times 10^{-6}$  in our sample) ensures that the Mg abundances used in the HEx ratio reliably trace the birth-gas composition. We prefer to use the Na-O anti-correlation as a tool to select the P stars because it is a signature present in the overwhelming majority of GCs, whereas significant Mg variations are biased towards massive and metal-poor GCs only (see

Section 1). Average abundances of the P component are listed in the second row in Table 1 for each GC.

### 3. The HEx ratio

Derived HEx ratios of hydrostatic to explosive  $\alpha$ -elements is shown in Fig. 2 as a function of metallicity for our sample of GCs. The ratio is computed from the mean  $([O/Fe] + [Mg/Fe])/2$  and  $([Si/Fe] + [Ca/Fe] + [Ti/Fe])/3$  for hydrostatic and explosive species, respectively. Red colour is used for in situ GCs and blue colour indicates accreted GCs. Empty grey circles are field galactic stars used as a comparison. The green square is the value for the stars in the nucleus of Sgr.

In the upper panel, the averages are done using all stars in GCs, regardless of the P, I, and E class, whereas in the lower panel we use only the unpolluted P component. The two panels

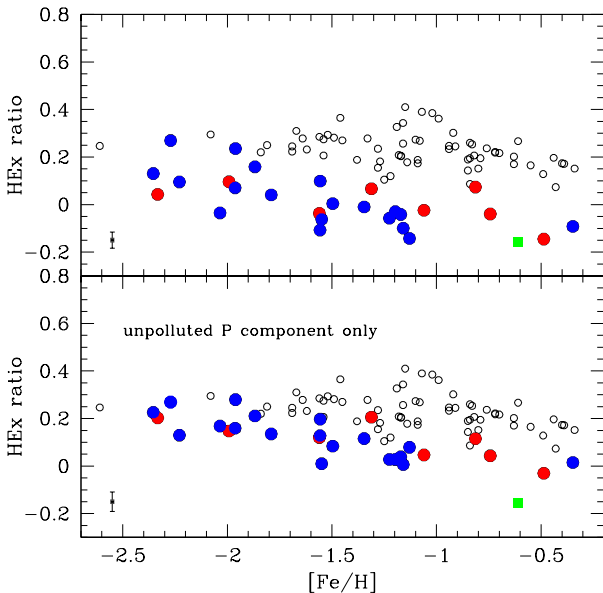


**Fig. 2.** The ratio of the average of hydrostatic  $\alpha$ -elements O and Mg to the average of explosive  $\alpha$ -elements Si, Ca, and Ti (HEx ratio) for our sample of GCs. In the lower panel the ratio is computed using only stars of the unpolluted P component in each GC (see text). Blue and red symbols are for accreted and in situ GCs, respectively, grey empty circles are field stars from Gratton et al. (2003). The green square is for field stars in the core of Sgr dSph. A typical error is shown in both panels (average from all GCs).

allow to discern at a glance the effect of the MP phenomenon. In GCs, O can be depleted by as much as 1 dex by proton-capture reactions at moderate temperature (20-40 MK, see e.g. Gratton et al. 2019), whereas the depletion in Mg is usually much smaller, requiring higher temperature for a significant variation. Compared to the reference field stars the HEx ratios in the upper panel are lower due to the large depletions in O and the moderate depletions in Mg in the polluted components I and E of GCs. When only the unpolluted component is used (lower panel) the HEx ratios are higher, closer to the locus of field stars.

In both panels the ratio is decreasing with increasing [Fe/H], irrespective of the origin (in situ or accreted) of GCs, in good agreement with results by HN25 from APOGEE. The HEx ratio for field stars in the Sgr nucleus is located below the plane defined by the GCs, in particular in the lower panel. Again, this is consistent with the overall lower ratio found by HN25 for satellite galaxies when compared to GCs. Field stars (empty circles) seems to show a pattern with a knee at [Fe/H]=-1 dex reminiscent of the classical plateau plus decrease displayed by individual  $\alpha$ -elements.

We note that Horta et al. (2020) claim that a difference exists between the mean level of [Si/Fe] for accreted and in situ subgroups of GCs at metallicity higher than about [Fe/H]=-1.5. However, in both HN25 and in the present study there is no dependence on the origin of the various groups of GCs. In the HEx ratio the weight given to Si is decreased by “diluting” the relevance of the [Si/Fe] ratio with four other  $\alpha$ -elements. These findings seem to corroborate the possible presence of problems in the analysis of Si in APOGEE, as suggested in Carretta (2026).

#### 4. Comparison with APOGEE results

Although the trend with [Fe/H] of the HEx ratio is broadly consistent with the results by HN25 and we agree that in our homogeneous dataset the locus of accreted and in situ GCs cannot be distinguished, we found a few relevant differences with APOGEE results. First, HN25 claim that NGC 7078 (M 15) is an outlier, with a low HEx ratio ( $\sim 0.1$ ) at  $[Fe/H] \sim -2.45$ . In our data M 15, with a HEx ratio 0.203 is well inside the region populated by the other metal-poor GCs (e.g. NGC 4590, NGC 7099, Ter 8).

Second, HN25 find for NGC 6715 (M 54) an HEx ratio very close to the value derived for the core of the Sgr galaxy, at  $[Fe/H] \sim -0.65$  dex. This is highly surprising, since the average metallicity of M 54 is  $-1.559^2$  ( $\sigma = 0.189$  dex, 76 stars) according to Carretta et al. (2010c), who also find a mean  $[Fe/H] = -0.622$  dex from the 27 stars in the Sgr nucleus surrounding M 54. Furthermore, the APOGEE results in Mészáros et al. (2020) give a mean metallicity  $[Fe/H] = -1.47$  ( $\sigma = 0.15$  dex) for M 54, again inconsistent with the value in HN25. To better understand the origin of the discrepancy, we cross-identified the 76 bona fide members of M 54 for radial velocity and abundance in Carretta et al. (2010c) with APOGEE DR17. We found 16 matches, with 6 stars flagged ASPFLAG=0 denoting reliable abundances. Three out of six are unpolluted stars, according to Carretta et al. (2010c). From them we derived  $[Fe/H] = -1.482$  dex and  $HEx = +0.140$ , in excellent agreement with the HEx sequence of GCs of similar metallicity. As a check, we next followed the procedure of HN25 by extracting from the value-added catalogue by Schiavon et al. (2024) all entries for NGC6715. We then applied all the selection criteria listed in Section 2 of HN25. The distribution of the metallicities from this selection is shown in Fig. 3, where the bulk is at [Fe/H] around -0.6 dex, consistent with the average metallicity for stars in the Sgr nucleus found in Carretta et al. (2010c). In HN25, both M 54 and Sgr seem to be located at this mean value of [Fe/H]. We hypothesise that probably the selection for the label NGC6715 provided mostly stars of the Sgr core (609 stars), in which the genuine globular cluster M 54 is immersed (the peak at -1.5 dex, 98 stars). The close values shown in HN25 are likely the result of this confusion. The genuine cluster M 54, whose stars show an extended Na-O anti-correlation (signature of a true GC), is much more metal-poor (Carretta et al. 2010c, Mészáros et al. 2020). At this metallicity, the hydrostatic and explosive  $\alpha$ -elements of its stellar population give a HEx ratio (+0.128 from our analysis) that places M 54 in the midst of the relation defined by GCs, being well distinct from the value (lower HEx ratio and higher metallicity) derived from field stars in the Sgr core (see Fig. 2). Moreover, in our dataset Terzan 8 (HEx=0.269), another GC associated to the Sgr dSph, is well located on the sequence of GCs for its metallicity and well separated from the Sgr field location.

#### 5. Discussion and conclusions

A large survey of  $\alpha$ -elements in GCs, recently completed, is exploited together with previous studies to assemble an extremely homogeneous dataset for abundances of hydrostatic and explosive elements in 27 GCs. From this set we computed the HEx ratio (Carlin et al. 2018) of hydrostatic (O, Mg) to explosive (Si, Ca, Ti) elements, using the primordial P component in GCs to disentangle the original ratios from the effects of MPs that alter

<sup>2</sup> This value is different from the one in Table 1 because is the average from the more large sample of GIRAFFE stars.

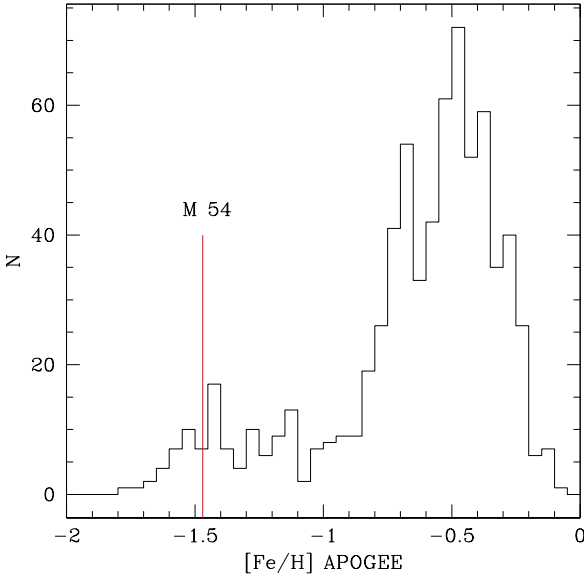


**Fig. 3.** Distribution of metallicities for stars labelled as candidate members of NGC6715 in Schiavon et al. (2024), after the selection cuts from Horta and Ness (2025). The mean metallicity from APOGEE (Mészáros et al. 2020) for M 54 is indicated by the vertical red line.

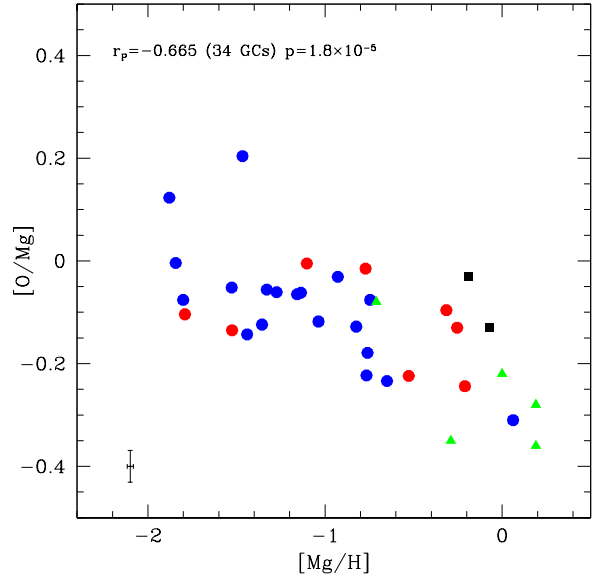


**Fig. 5.** Abundance ratio [O/Mg] as a function of [Mg/H] for the extended sample of GCs. Symbols are as in Fig. 4.

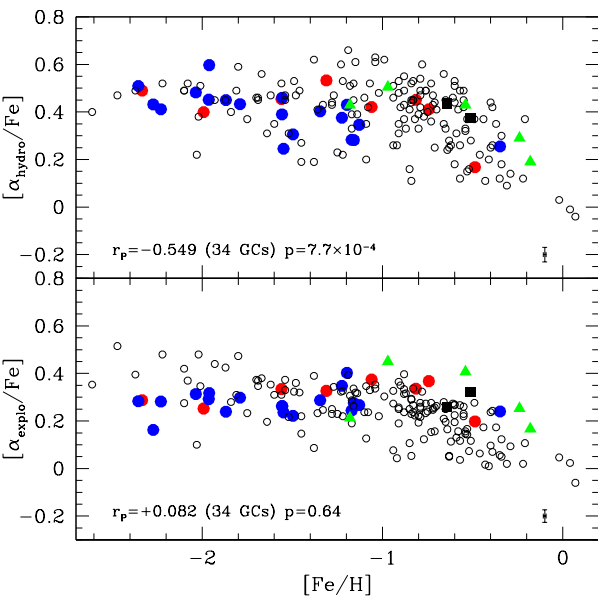


**Fig. 4.** Abundance ratios of the hydrostatic (upper panel) and explosive (lower panel)  $\alpha$ -elements in the GCs of our extended sample. Blue and red points indicate accreted and in situ GCs. Black squares are disk GCs and green triangles are bulge GCs from literature. The Pearson's correlation coefficient and two-tailed probability are listed. Only Mg is used to represent the hydrostatic species in field stars.

predominantly the abundances of O, but also those of Mg, Si, and sometimes Ca (see e.g. Carretta 2026).

In general, despite a few discrepant cases, we confirm with high resolution optical spectroscopy the main results obtained by HN25 using the near-infrared spectroscopic survey APOGEE. In the plane mapping the HEx ratio as a function of metallicity, the GCs cannot be distinguished by their in situ or accreted origin. In this plane, the sequence of GCs born in the main body of the Milky Way is superimposed to the sequence of GCs though

to be formed in external systems. Both sequences lie about 0.1 dex above the locus occupied by satellite galaxies. In our study, we have only one comparison represented by stars in the Sgr dSph core, for reasons of homogeneity in the abundance analysis. However, this finding is supported by the much larger sample of galaxies and halo substructures shown in HN25.

We also confirm that the HEx ratios of GCs decrease as the metallicity increases, as shown in HN25. The observed gradient with [Fe/H] can be explained following the two scenarios first discussed by McWilliam et al. (2013) to account for the variation of the [Mg/Ca] ratio over the metallicity range of the Sgr dSph field stars. The HEx ratio measures the contribution to  $\alpha$ -elements by hydrostatic burning in massive stars compared to the yield from all the stars exploding as SNe events. The two scenarios affect respectively the numerator and the denominator of the HEx ratio.

A lower HEx ratio may imply a smaller contribution to the enrichment by the most massive stars ( $M > 8M_{\odot}$ ) among the SN II progenitors, that is a top light (bottom heavy) IMF like that typical of low mass satellite galaxies of the Milky Way. This scenario explains the position of dwarf galaxies in the HEx ratio - [Fe/H] plane, systematically located at lower HEx ratios with respect to GCs at any metallicity (see HN25, and also the value for Sgr in Fig. 2 of the present paper).

Alternatively, a lower HEx ratio may result from changing the factors that control the denominator, for example an excess of type Ia SNe. An increased contribution to the nucleosynthesis as metallicity increases will raise both [Fe/H] and the content of Si, Ca, and Ti, whereas the production of hydrostatic elements is expected to be negligibly low (e.g. Nomoto et al. 1984). This is the explanation preferred by HN25 to account for the trend with metallicity observed for the HEx ratio in GCs.

On the other hand, in a single dSph, Sgr, Carlin et al. (2018) found that the abundance ratios of hydrostatic elements were located much further below the MW stars used as reference than the abundance ratios of elements produced in explosive nucleosynthesis, suggesting a IMF lacking the most massive SN II progenitors.

It seems to be even more difficult to use a delayed SNe Ia mechanism to explain the decreasing HEx ratio with metallicity for GCs that are originated in different environments. The chemodynamics and the age-metallicity relations of GCs in Fig. 2 indicates that they come from five or six galaxies (Massari et al. 2019), i.e. the Milky Way disc and bulge, Gaia-Enceladus, Sequoia, Sgr, and the progenitors of the Helmi Stream and low-energy GCs, later injected in the Milky Way following the accretion events. It would be hard to imagine that the SNe Ia contribution worked to place exactly on the same relation of declining HEx ratio GCs formed in systems with different global masses, star formation rates, and thus different timescales for the prompt and delayed enrichment from SNe.

The two alternative scenarios can be tested by looking separately at the trends with the metallicity of each of the two terms of the HEx ratio,  $[\alpha_{\text{hydro}}/\text{Fe}]$  and  $[\alpha_{\text{explo}}/\text{Fe}]$ , as done in Fig. 4. For this figure we employed again only the average values derived from the primordial P component in each GC, to remove the effect of MPs on the ratios. We adopt only Mg as representative of hydrostatic species in field stars to increase the sample size. To better sample the critical region at high metallicity ( $[\text{Fe}/\text{H}] \gtrsim -1$  dex) where the bulk of SNe Ia is expected to manifest, we added to our sample GCs from literature. We included five bulge GCs (green triangles in Fig. 4) and two disc GCs (black squares), all with abundances derived from high resolution optical spectra. The added GCs are NGC 6553, NGC 6528, NGC 6440 (Muñoz et al. 2020, 2018, 2017), NGC 6723 (Crestani et al. 2019), NGC 6522 (Barbuy et al. 2021), NGC 5927 (Mura-Guzmán et al. 2018), and NGC 6366 (Puls et al. 2018). All abundances were corrected to our solar abundance scale. The stars analysed in these GCs are often less than 10, hence we could not safely apply the classification by Carretta et al. (2009c) to extract the unpolluted component. However, in these metal-rich GCs the Na-O anti-correlation has an almost vertical trend (e.g. Muñoz et al. 2020), with no significant spread in O, and the Mg-Al anti-correlation, with significant Mg depletions, is not observed in metal-rich GCs (Carretta et al. 2009a, Mészáros et al. 2020).

We applied a linear regression to the extended sample of GCs in Fig. 4. We list in the panels the Pearson's correlation coefficient and the two-tailed probability testing the null hypothesis that the observed value comes from a population in which the true correlation is zero. In the lower panel of Fig. 4 the (weak) correlation of the ratio  $[\alpha_{\text{explo}}/\text{Fe}]$  as a function of metallicity is not statistically significant, meaning that the level of explosive  $\alpha$ -elements is almost constant in all GCs over the whole metallicity range. Instead, the effect due to the time delay between core-collapse and SNe Ia as detailed by Tinsley (1979) is clearly visible in the reference field stars after about  $[\text{Fe}/\text{H}] = -1$  dex, the region where stars enter the high-Ia regime. This terminology, mutated from Griffith et al. (2019), is more appropriate to highlight that the ratio in field stars is decreasing due to the increasing contribution of Fe from SNe Ia that effectively does lower the plateau established by core-collapse SNe. This lowering is not apparent among GCs, with  $[\alpha_{\text{explo}}/\text{Fe}]$  remaining constant over an interval of about 2 dex in  $[\text{Fe}/\text{H}]$ .

What is definitely changing with regularity in GCs, already at low metallicity, is the content of hydrostatic species (upper panel in Fig. 4). The linear regressions listed in Fig. 4 shows a statistically significant trend with  $[\text{Fe}/\text{H}]$ . This decline is suggesting that the impact on the HEx ratio is due to a variation of the properties of the most massive stars ( $15-30 M_{\odot}$ ).

The irrelevance of contributions from SNe Ia can be better appreciated from Fig. 5 where we plot the ratio  $[\text{O}/\text{Mg}]$  of the

elements produced in the hydrostatic cores of massive stars as a function of metallicity. We here adopt the ratio  $[\text{Mg}/\text{H}]$  as reference for metallicity because Mg is produced almost entirely by core-collapse SNe while Fe is provided both in SNe II and Ia. Using  $[\text{Mg}/\text{H}]$ <sup>3</sup> the effect of SN Ia to the enrichment is not contained in this plot (e.g. Gratton et al. 1996, 2000; Furhman 1998).

Despite O and Mg being produced by the same stars on similar timescales, the ratio  $[\text{O}/\text{Mg}]$  is not flat, but decreases with metallicity and the relation has high statistical significance. The expected yields of hydrostatic elements increase rapidly with progenitor mass (e.g. Woosley and Weaver 1995) and with such a strong sensitivity to SN mass, the IMF would impact on the abundance ratios. At constant mass the metallicity dependence is weak (see Andrews et al. 2017), however the IMF-averaged yields may depend on metallicity if the IMF changes as a function of metallicity, increasing the fraction of low-mass SNe toward higher metallicity (a more top-light IMF). The decline of  $[\text{O}/\text{Mg}]$  with increasing  $[\text{Mg}/\text{H}]$  would be then explained preferentially by a deficit in the highest mass stars for the more metal-rich GC population.

There are several studies pointing to a metallicity dependent IMF for GCs. For instance, Marks et al. (2012) found that the lower the cluster metallicity, the more top heavy the IMF must have been, since the high mass IMF slope is required to be linearly correlated with metallicity in order to remove residual gas from the proto-GC shortly after the initial star formation. The same conclusion was reached by Wirth et al. (2022) with analytical models tailored to investigate the observed iron spreads in GCs. They found that all GCs had IMFs more top-heavy than the canonical one, and that a lower metallicity decreases the high mass slope making the GC more top-heavy. The HEx and  $[\text{O}/\text{Mg}]$  ratios, declining with increasing metallicity, support these studies, agreeing with a scenario with an IMF that lacks more and more massive stars as  $[\text{Fe}/\text{H}]$  increases, with no compelling need of a significant contribution of Type Ia supernova pre-enrichment.

Finally, at odds with HN25, we find a statistically significant relation between the HEx ratio and the total present-day mass of GCs, using as proxy the total absolute luminosity (Fig. 6, left panel), with the ratio decreasing for higher mass GCs. The regression is significant using both our extended sample (upper row label in the panel) and our original sample of GCs. Again, this correlation is only due to the variation in the content of the elements produced in hydrostatic burning (middle panel in Fig. 6), whereas the  $[\alpha_{\text{explo}}/\text{Fe}]$  ratio remains constant (right panel).

Present day masses could not be the best choice for objects like GCs, formed in a variety of different environments and subjected to the effects of dynamical evolution for almost an Hubble time. However, it seems that the relation between the HEx ratio and the mass is imprinted since the epoch of the GC formation. Indeed, we found a statistically significant decrease of the HEx ratio also as a function of increasing initial GC masses (estimated by Baumgardt et al. 2019), as shown in Fig. 7, again in contrast with results from HN25, who do not find any correlation with GC mass.

We speculate that the decline with total mass could be a reflection of the weak correlation between mass and metallicity among GCs, since the most massive objects are preferentially closer to the central regions of the Galaxy, where it is more

<sup>3</sup> Our results would be the same by using  $[\text{O}/\text{H}]$  instead.

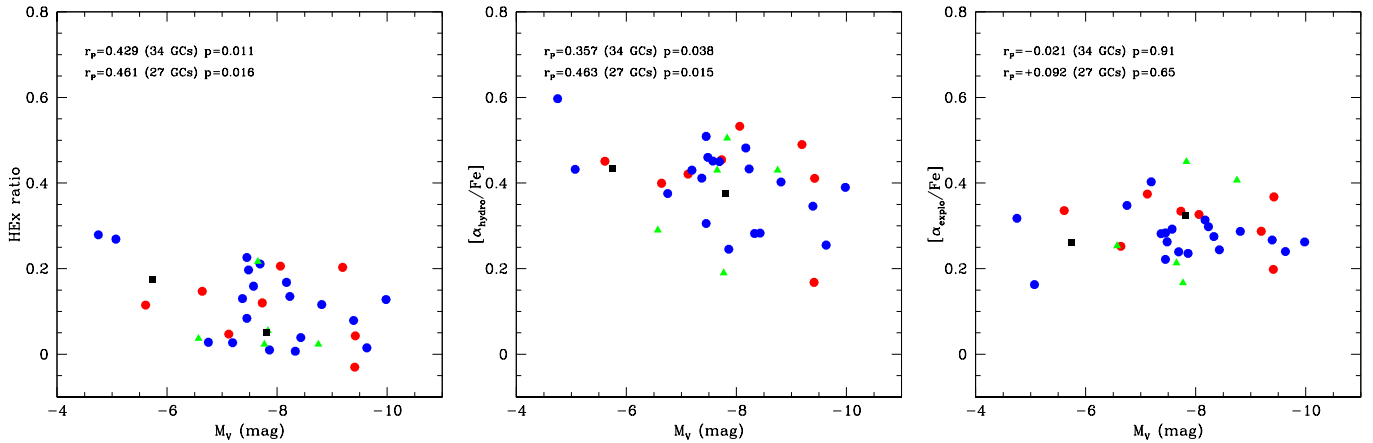


**Fig. 6.** The HEx ratio (left panel), the  $[\alpha_{\text{hydro}}/\text{Fe}]$  (middle panel), and the  $[\alpha_{\text{explo}}/\text{Fe}]$  ratio (right panel) as a function of the global absolute luminosity of GCs (Harris 2010). The results of the linear regression are referred to the extended sample (upper row) and to our original sample (lower row). Symbols are as in Fig. 4.

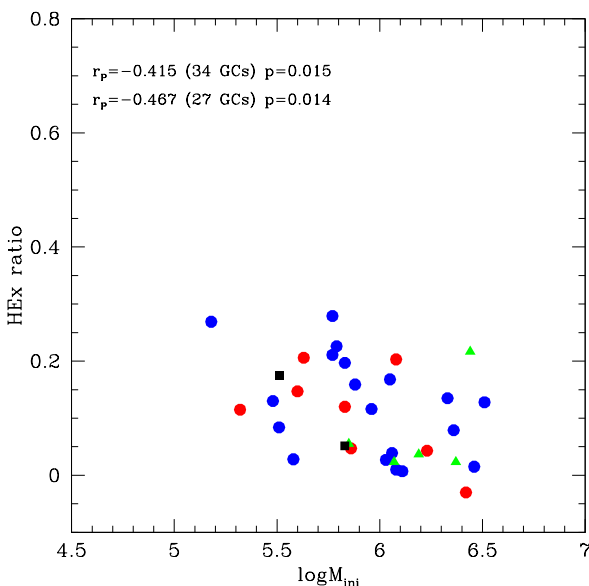


**Fig. 7.** The HEx ratio as a function of the initial GC mass from Baumgardt et al (2019). Symbols are as in Fig. 4.

probable to find metal-rich objects (see e.g. the univariate correlations in figure 5 of Baumgardt et al. 2019).

To summarise, all the signatures we found in the present work (the declining ratio  $[\text{O}/\text{Mg}]$  as a function of  $[\text{Mg}/\text{H}]$ , the HEx ratio decreasing with increasing metallicity, and with initial and present day mass of GCs) would seem to support a coherent picture where a IMF changing with metallicity may explain the observed correlations. Even if the IMF in the high mass regime can never be directly observed in present day GCs, the content of different  $\alpha$ -elements incorporated in the stars we can access today can be efficiently used to probe the ephemeral first phases of GC evolution.

**Acknowledgements.** This research has made large use of the SIMBAD database (in particular Vizier), operated at CDS, Strasbourg, France, of the NASA's Astrophysical Data System, and TOPCAT (Taylor 2005). I especially thanks Angela Bragaglia and Donatella Romano for several valuable suggestions. I also acknowledge funding from Bando Astrofisica Fondamentale INAF 2023 (PI A. Vallenari) and from Prin INAF 2019 (PI S. Lucatello).

## References

Andrews, B.H., Weinberg, D.H., Schonrich, R., Johnson, J.A. 2017, *ApJ*, 835, 224  
 Arnould, M., Goriely, S., Jorissen, A. 1999, *A&A*, 347, 572  
 Barbuy, B., Cantelli, E., Muniz, L. et al. 2021, *A&A*, 654, A29  
 Baumgardt, H., Hilker, M., Sollima, A., Bellini, A. 2019, *MNRAS*, 482, 5138  
 Bragaglia, A., Carretta, E., D'Orazi, V. et al. 2017, *A&A*, 607, A44  
 Burbidge, E.M., Burbidge, G.R., Fowler, W.A., Hoyle, F. 1957, *Rev.Mod.Phys.*, 29, 547  
 Carlin, J.L., Sheffield, A.A., Cuhna, K., Smith, V.V. 2018, *ApJ*, 859, L10  
 Carretta, E. 2013, *A&A*, 557, A128  
 Carretta, E. 2015, *ApJ*, 810, 148  
 Carretta, E. 2026, in press on *A&A*  
 Carretta, E., Bragaglia, A. 2021, *A&A*, 646, A9  
 Carretta, E., Bragaglia, A. 2022, *A&A*, 659, A122  
 Carretta, E., Bragaglia, A. 2023, *A&A*, 677, A73  
 Carretta, E., Bragaglia, A., Gratton, R.G. et al. 2007a, *A&A*, 464, 939  
 Carretta, E., Bragaglia, A., Gratton, R.G., Lucatello, S., Momany, Y. 2007b, *A&A*, 464, 927  
 Carretta, E., Bragaglia, A., Gratton, R.G., Lucatello, S. 2009a, *A&A*, 505, 139  
 Carretta, E., Bragaglia, A., Gratton, R.G., D'Orazi, V., Lucatello, S. 2009b, *A&A*, 508, 695  
 Carretta, E., Bragaglia, A., Gratton, R.G. et al. 2009c, *A&A*, 505, 117  
 Carretta, E., Bragaglia, A., Gratton, R.G. et al. 2010a, *A&A*, 516, 55  
 Carretta, E., Bragaglia, A., Gratton, R.G. et al. 2010b, *ApJ*, 712, L21  
 Carretta, E., Bragaglia, A., Gratton, R.G. et al. 2010c, *A&A*, 520, 95  
 Carretta, E., Lucatello, S., Gratton, R.G., Bragaglia, A., D'Orazi, V. 2011, *A&A*, 533, 69  
 Carretta, E., Bragaglia, A., Gratton, R.G., Lucatello, S., D'Orazi, V. 2012, *ApJ*, 750, L14  
 Carretta, E., Gratton, R.G., Bragaglia, A., D'Orazi, V., Lucatello, S. 2013a, *A&A*, 550, A34  
 Carretta, E., Bragaglia, A., Gratton, R.G. et al. 2013b, *A&A*, 557, A138  
 Carretta, E., Bragaglia, A., Gratton, R.G. et al. 2014a, *A&A*, 564, A60  
 Carretta, E., Bragaglia, A., Gratton, R.G. et al. 2014b, *A&A*, 561, A87  
 Carretta, E., Bragaglia, A., Gratton, R.G. et al. 2015, *A&A*, 578, A116  
 Carretta, E., Bragaglia, A., Lucatello, S. et al. 2017, *A&A*, 600, A118  
 Crestani, J., Alves-Brito, A., Bono, G., Puls, A.A., Alonso-Garcia, J. 2019, *MNRAS*, 487, 5463  
 Fuhrmann, K. 1998, *A&A*, 338, 161  
 Gratton, R., Carretta, E., Matteucci, F., Sneden C. 1996, *ASPC*, 92, 307  
 Gratton, R., Carretta, E., Matteucci, F., Sneden C. 2000, *A&A*, 358, 671  
 Gratton, R.G., Carretta, E., Claudi, R., Lucatello, S., Barbieri, M. 2003, *A&A*, 404, 187  
 Gratton, R.G., Sneden, C., Carretta, E. 2004, *ARA&A*, 42, 385  
 Gratton, R.G., Lucatello, S., Bragaglia, A. et al. 2006, *A&A*, 455, 271  
 Gratton, R.G., Lucatello, S., Bragaglia, A. et al. 2007, *A&A*, 464, 953  
 Gratton, R.G., Carretta, E., Bragaglia, A. 2012, *A&ARv*, 20, 50  
 Gratton, R.G., Bragaglia, A., Carretta, E. et al. 2019, *A&ARv*, 27, 8  
 Griffith, E., Johnson, J.A., Weinberg, D.H. 2019, *ApJ*, 886, 84  
 Harris, W.E. 2010, arXiv:1012.3224  
 Horta, D., Ness, M.K. 2025, *MNRAS*, 544, L64

Horta, D., Schiavon, R.P., Mackereth, J.T. et al. 2020, MNRAS, 493, 3363  
 Langer, G.E., Hoffman, R., Sneden, C. 1993, PASP, 105, 301  
 Marks, M., Kroupa, P., Dabringhausen, J., Pawlowski, M.S. 2012, MNRAS, 422, 2246  
 Massari, D., Koppelman, H.H., Helmi, A. 2019, A&A, 630, L4  
 McWilliam, A., Wallerstein, G., Mottini, M. 2013, ApJ, 778, 149  
 Mészáros, S., Masseron, T., García-Hernández, D.A. et al. 2020, MNRAS, 492, 1641  
 Muñoz, C., Villanova, S., Geisler, D. et al. 2017, A&A, 605, A12  
 Muñoz, C., Geisler, D., Villanova, S. et al. 2018, A&A, 620, A96  
 Muñoz, C., Villanova, S., Geisler, D. et al. 2020, MNRAS, 492, 3742  
 Mura-Guzmán, A., Villanova, S., Muñoz, C. 2018, MNRAS, 474, 4541  
 Nomoto, K., Thielemann, F.-K., Yokoi, K. 1984, ApJ, 286, 644  
 Puls, A.A., Alves-Brito, A., Campos, F., Dias, B., Barbuy, B. 2018, MNRAS, 476, 690  
 Schiavon, R.P., Phillips, S.G., Myers, N. et al. 2017, MNRAS, 528, 1393  
 Taylor, M.B. 2005, Astronomical Data Analysis Software and Systems XIV, 347, 29  
 Tinsley, B.M. 1979, ApJ, 229, 1046  
 Wallerstein, G. 1962, ApJS, 6, 407  
 Weinberg, D.H., Holtzman, J.A., Hasselquist, S. et al. 2019, ApJ, 874, 102  
 Wirth, H., Kroupa, P., Haas, J. et al. 2022, MNRAS, 516, 3342  
 Woosley, S.E., Weaver, T.A. 1995, ApJS, 101, 181  
 Yong, D., Grundahl, F., Nissen, P.E., Jensen, H.R., Lambert, D.L. 2005, A&A, 438, 875

## Appendix A: References for the data on globular clusters

In the following table we provide a synopsis of all the papers where the original data on abundances can be retrieved for individual stars in GCs, usually in electronic form at CDS.

**Table A.1.** References for GC abundances used in this work

GC	[O/Fe]	[Mg/Fe]	[Si/Fe]	[Ca/Fe]	[Ti/Fe] 1	[Fe/H]
0104	1,2	2,3	2,3	4,5	5	6
0288	1,2	2,5	2,5	4,5	5	6
0362	7	7	7	7	7	7
1851	8	8	8	8	8	8
1904	1,2	2,5	2,5	4,5	5	6
2808	9	9	9	9	9	9
3201	1,2	2,5	2,5	4,5	5	6
4590	1,2	2,5	2,5	4,5	5	6
4833	10	10	10	10	10	10
5634	11	11	11	11	11	11
5904	1,2	2,5	2,5	4,5	5	6
6093	12	12	12	12	12	12
6121	1,2	2,3	2,3	4,5	5	6
6171	1,2	2,5	2,5	4,5	5	6
6218	2,13	2,5	2,5	4,5	5	6
6254	1,2	2,5	2,5	4,5	5	6
6388	14	14	14	14	14	15
6397	1,2	2,5	2,5	4,5	5	6
6441	16	16	16	16	16	16
6535	17	17	17	17	17	17
6715	18	18	18	18	18	18
6752	2,19	2,20	2,20	4,5	5	6
6809	1,2	2,5	2,5	4,5	5	6
6838	1,2	2,5	2,5	4,5	5	6
7078	1,2	2,5	2,5	4,5	5	6
7099	1,2	2,5	2,5	4,5	5	6
Ter8	21	21	21	21	21	21

- 1=Carretta et al. (2009b), 2=Carretta et al. (2009a), 3=Carretta et al. (2013a)
- 4=Carretta et al. (2010b), 5=Carretta (2026, in press), 6=Carretta et al. (2009c)
- 7=Carretta et al. (2013b), 8=Carretta et al. (2011), 9=Carretta (2015)
- 10=Carretta et al. (2014a), 11=Carretta et al. (2017), 12=Carretta et al. (2015)
- 13=Carretta et al. (2007a), 14=Carretta and Bragaglia (2023), 15=Carretta and Bragaglia (2022)
- 16=Gratton et al. (2006,2007), 17=Bragaglia et al. (2017), 18=Carretta et al. (2010c)
- 19=Carretta et al. (2007b), 20=Carretta et al. (2012), 21=Carretta et al. (2014b)
- Based on observations collected at ESO telescopes under programmes 072.D-0507, 073.D-0211, 073.D-0.760, 081.D-286, 381.D-0329, 083.D-0208, 085.D-0205, 087.B-0086, 093.B-0.583, 095.D-0834, 099.D-0047.